JGR Space Physics

RESEARCH ARTICLE
10.1029/2019JA027319

Pc4-5 Poloidal ULF Wave Observed in the Dawnside Plasmaspheric Plume

Shuai Zhang[1,2], Anmin Tian[1], Alexander W. Degeling[1], Quanqi Shi[1], Mengmeng Wang[1], Yixin Hao[3], Jie Ren[3], Wenlong Liu[4], Xuzhi Zhou[3], Xiao-Chen Shen[5], Weijie Sun[6], I. Jonathan Rae[7], and Shichen Bai[1]

[1]Shandong Provincial Key Laboratory of Optical Astronomy and Solar-Terrestrial Environment, Institute of Space Sciences, Shandong University, Weihai, China, [2]State Key Laboratory of Space Weather, Chinese Academy of Sciences, Beijing, China, [3]School of Earth and Space Sciences, Peking University, Beijing, China, [4]Space Science Institute, School of Astronautics, Beihang University, Beijing, China, [5]Center for Space Physics, Boston University, Boston, MA, USA, [6]Department of Climate and Space Sciences and Engineering, University of Michigan, Ann Arbor, MI, USA, [7]Space and Climate Physics, Mullard Space Science Laboratory, University College London, Dorking, UK

Abstract A localized Pc4-5 ultralow-frequency (ULF) wave event associated with a plasmaspheric plume was observed by THEMIS-E on the dawnside near $L = 6$, which was identified as a second harmonic poloidal wave. The plume was identified as a sudden density enhancement during an outbound pass. The charged particle populations in the plume have a variety of periodic modulation characteristics at different energies. First, there is an antiphase relationship between magnetic field *Br* and particle flux across a wide energy range both for ions and electrons (~50 keV to 1 MeV). Second, there is a 180° phase shift in the modulated ion flux within an energy range of ~2–6 keV, with negative slope dispersions of ion pitch angle distributions at ~2–6 keV and ~50–75 keV, which are characteristic of drift-bounce resonances. Third, the lower-energy (<32 eV) ion flux is modulated at double the wave frequency, which are the result of $E \times B$ effect. Considering the generation mechanism of this poloidal mode wave within the plume, we find that it is likely generated by drift-bounce resonance from an unstable population of ions, due to an inward radial phase space density gradient. We suggest that the localization of waves to the plume is because the high plasma density reduces the local poloidal mode eigenfrequency, enabling a match to the drift-bounce frequencies of these ions, and resonant energy transfer from these particles to the eigenfunction at this location. This generates the Pc4-5 second harmonic poloidal waves at a much lower *L* region than would otherwise be expected.

Key Points:
- The high-*m* poloidal waves in the dawnside plume were observed by THEMIS-E
- The inward radial gradient of ~57 keV and higher plasma density enable the second harmonic poloidal wave to occur in the dawnside plume
- Three types of particle flux modulations are observed simultaneously along with the wave in different energy bands

Supporting Information:
- Supporting Information S1

Correspondence to:
A. Tianand A. W. Degeling,
tamin@sdu.edu.cn;
degeling@sdu.edu.cn

Citation:
Zhang, S., Tian, A., Degeling, A. W., Shi, Q., Wang, M., Hao, Y., et al. (2019). Pc4-5 Poloidal ULF Wave Observed in the Dawnside Plasmaspheric Plume. *Journal of Geophysical Research: Space Physics*, *124*, 9986–9998. https://doi.org/10.1029/2019JA027319

Received 22 AUG 2019
Accepted 31 OCT 2019
Accepted article online 15 NOV 2019
Published online 06 DEC 2019

1. Introduction

The Earth's plasmasphere consists of cold, dense plasma from the ionosphere. The dynamics of the plasmasphere can be understood by considering the balance between source and loss processes, due to ion outflow from the ionosphere and transport to the magnetopause, respectively. This transport is in turn understood by a balance of competing processes, namely, corotation with the Earth's rotational motion, and magnetospheric convection, driven by dayside and nightside magnetic reconnection rates. During intervals of strong convection during geomagnetic storms, the dayside outer plasmasphere surges outward by enhanced sunward convection, forming a plasmaspheric drainage plume in the dusk sector, which transports the cold plasma from the plasmasphere to the dayside magnetopause. Under sustained strong convection this structure can become increasingly narrow and localized to the afternoon sector as the remnant of the outer plasmasphere is gradually lost to the magnetopause. Then, as sunward convection weakens during the storm recovery phase, the remnant plume, now a narrow filamentary structure, corotates eastward with the Earth and becomes wrapped around nightside and morning sector (e.g., Fu & Sun, 2016; Goldstein et al., 2005; Spasojević et al., 2003). The plasmaspheric plume is usually detected as a “detached plasma” region, which is a distinctly isolated region with sudden and significant increase in the total plasma density (e.g., Chappell, 1974; Chappell et al., 1970).

The Pc4-5 ultralow-frequency (ULF) waves are electromagnetic oscillations in the Earth's magnetosphere with frequency between ~1 and 22.2 mHz. According to whether the magnetic field perturbations are in the radial or azimuthal directions, they are classified as toroidal or poloidal mode. Pc4-5 toroidal waves

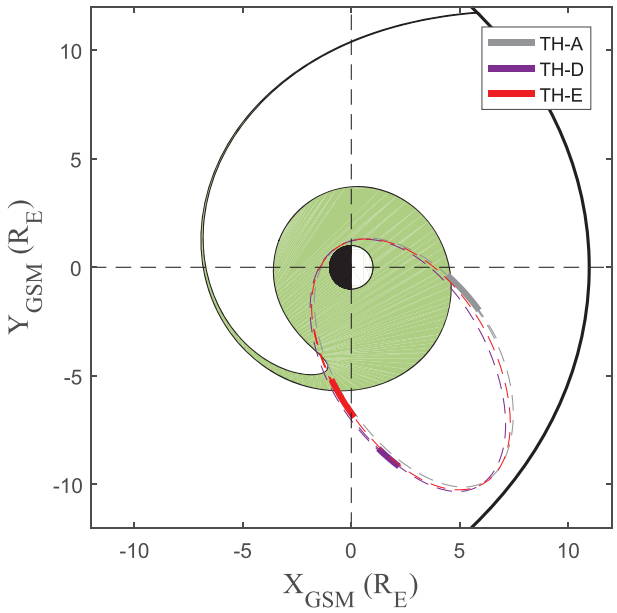

Figure 1. Orbits of TH-A (gray), TH-D (purple), and TH-E (red) in the GSM *X-Y* plane during 01:00–02:10 UT on 22 March 2013 are marked by the thick solid lines. The dashed curves represent the orbits of the whole day. The magnetopause is plotted based on the Shue et al. (1998) model with the averaged solar wind dynamic pressure = 1.37 nPa and IMF *Bz* = 5.8 nT. The green region indicates the plasmaspheric plume region at 01:00 UT on 22 March 2013, derived from the plasmapause test particle simulations of Goldstein et al. (2014).

with low *m* are usually considered to be caused by external sources, such as Kelvin-Helmholtz instability along the magnetopause (e.g., Claudepierre et al., 2008; Ling et al., 2018; Rae et al., 2005; Zhang et al., 2018), solar wind dynamic pressure impulse (e.g., Allan et al., 1986; Degeling et al., 2014; Lee & Lysak, 1989; Shen et al., 2015, 2017; Shi et al., 2013, 2014; Tian et al., 2016; Zong et al., 2012), and foreshock transients (e.g., Hartinger et al., 2013; Shen et al., 2018). Pc4-5 poloidal waves with high wave number are usually driven by localized kinetic plasma instabilities such as the drift-bounce resonance instability (e.g., Oimatsu et al., 2018; Southwood, 1976; Yang et al., 2010), the free energy could be generally provided by bump-on-tail distribution at low-energy (~1–10 keV; e.g., Liu et al., 2013; Shi et al., 2018; Takahashi et al., 2018) or inward gradient of ion phase space density (PSD) at high energy (tens to hundreds of keV; e.g., Dai et al., 2013; Min et al., 2017; Yamamoto et al., 2018).

Alfvénic standing waves are characterized by a 90° phase difference between the electric field and magnetic field components (e.g., Singer et al., 1982). The sign of phase delay can be used to diagnose the harmonics mode of Pc4-5 ULF waves; for instance, the poloidal mode could be second harmonic (fundamental) wave if the phase of the radial magnetic field *Br* leads (lags) the azimuthal electric field *Ea* by 90°, if measured slightly south of the magnetic equator (e.g., Hao et al., 2014; Liu et al., 2013; Takahashi et al., 2011, 2014; Zhang et al., 2018). For poloidal mode waves, the second harmonic mode is the most common phenomenon in the Earth's magnetosphere, which is usually observed on the duskside near L ~ 5–6 with frequency in Pc4 band (6.7–22.2 mHz; e.g., Dai et al., 2015). Occasionally, fundamental poloidal waves are also observed in the dawnside magnetosphere near L ~ 5–6 with frequency in Pc4 and Pc5 bands (1–6.7 mHz) and have been identified as giant pulsations on the ground (e.g., Glassmeier et al., 1999; Rostoker et al., 1979; Takahashi et al., 2011; Wang et al., 2018).

In this paper, we present a 6.7 mHz (the boundary between the Pc4 and Pc5 bands) second harmonic poloidal ULF wave event near L ~ 6 in the dawnside plasmaspheric plume. We find that the observed poloidal oscillations are associated with a variety of periodic particle modulations at different energies and are likely generated by drift-bounce resonance of ions with an inward radial gradient of the PSD. In addition, we also confirmed the controlling effect of the plasmaspheric plume in the generation of Pc4-5 ULF wave.

The remainder of this paper is organized as follows. In section 2, we introduce the data set and the satellite orbits used in this study. In section 3, we present the satellite observations. In section 4, we discuss the wave-particle modulations and generation mechanism of the wave. Section 5 gives the main conclusions.

2. Data Set and Orbit

The magnetospheric measurements used in this study are mainly from the THEMIS mission, which consists of five identical satellites (TH-A, B, C, D, and E) with orbital inclination of about 10° (Angelopoulos, 2008). We use ~3 s resolution spin-fit magnetic field data from the fluxgate magnetometer (Auster et al., 2008), ~3 s resolution ion (5 eV to 25 keV) and electron (6 eV to 30 keV) data from the electrostatic analyzer (ESA; McFadden et al., 2008), ~3 s resolution ion (25 keV to 6 MeV) and electron energy fluxes (25 keV to 900 keV) from the solid state telescope (SST; Larson et al., 2008), and electric field data and spacecraft potential data from the electric field instrument (Bonnell et al., 2008). The ESA provides 22.5° × 11.25° inherent angular resolution (~22.5° pitch angle resolution) over 4 str. The SST provides 30° × 11.25° inherent angular resolution (~22.5° pitch angle resolution) over 3 str (Angelopoulos, 2008). Figure 1 shows the orbits of TH–A, TH–D, and TH–E in the GSM *X-Y* plane. The waves in the plume are observed by TH-E, whose orbit was outbound in the morning sector (the radial distance $R \approx 5.3$–7 R_E, MLT ≈ 5.3–6.1 hr, MLAT ≈ −11°) during 01:00–02:10 UT on 22 March 2013. The results of the test particle code by Goldstein et al. (2014), showing the simulated plasmapause location during this event, were used in Figure 1 and are publicly available online

(http://enarc.space.swri.edu/PTP/). These results provide an estimate of the time-varying global plasmapause location in 15 min time steps over a time range from 2012 to 2015, based on the solar wind data and *Kp* geomagnetic index.

A local field-aligned-cartesian (FAC) coordinate system with parallel (**z**), azimuthal (***a***), and radial (**r**) components is used to study waves, which is defined by

$$\mathbf{z} = \frac{\boldsymbol{B}_0}{|\boldsymbol{B}_0|}; \boldsymbol{a} = \frac{\boldsymbol{z}\times\boldsymbol{R}}{|\boldsymbol{z}\times\boldsymbol{R}|}; \boldsymbol{r} = \boldsymbol{a}\times\boldsymbol{z} \quad (1)$$

where $\boldsymbol{B_0}$ is derived by taking a 20 min running average of the magnetic field data and $\boldsymbol{R}$ is the outward position vector from Earth's center to the satellite.

3. Observation

3.1. The Pc4-5 Poloidal Wave in the Dawnside Plume

Figure 2 is an overview of this wave event. Figure 2a shows the electron density derived from spacecraft potential measurements. A density enhancement over the radial distance range from 5.3 to 7 R_E is observed, suggesting the presence of a plasmaspheric plume, which is also in good morphological agreement with the plume model shown in Figure 1. Figures 2b–2j show the magnetic field, velocity, and electric field components in the FAC coordinate system; all these components show clear wave characteristics. Figures 2k–2s show the PSD of the components in corresponding left Figures 2b–2j, which are derived by the fast Fourier transform analysis. We can see that there is an obvious single spectral peak at 6.7 mHz for each panel, and the PSD of the wave components *Br*, *Vr*, and *Ea* dominate over the other components. Therefore, this event is considered a quasi-monochromatic poloidal Pc4-5 wave event. One of the interesting features is that this wave exists after the TH-E enters into the plume region (two black vertical lines in left panels), which suggests that the ULF wave event is likely associated with the plasmaspheric plume. Furthermore, a minor geomagnetic storm with a minimum *Dst* value of −54 nT occurred about 1.5 days before this event, which may be the reason that the plume was observed in the dawnside as introduced in section 1.

3.2. Energy Spectrum and Particle Flux

Figures 3a and 3b show the omnidirectional ion energy spectrum measured from the SST (25 keV to 6 MeV) and ESA (5 eV to 25 keV) at 01:00–02:10 UT, respectively. We can see that there are three different modulations in higher, middle, and lower energies. The line plot in Figures 3e–3g show the omnidirectional ion flux at different energies, providing more clear information for these modulations as follows. Figure 3e shows antiphase modulations between *Br* and higher-energy ions (>50 keV); the characteristics of drift-bounce resonance (180° phase shift) at ~2–6 keV are shown in Figure 3f (Southwood & Kivelson, 1981; Zhou et al., 2016); and double peaks at lower energy (<32 eV) are shown in panel g, which could be the result of *E* cross *B* effect (Hirahara et al.,2004; Sakurai et al., 2014). In addition, Figures 4c and 4d show the electron energy spectrum measured by SST (30 to 900 keV) and ESA (6 to 30 keV), respectively. There is also an antiphase modulation between *Br* and higher-energy electrons (30 to 700 keV), although the line plots are not shown here. Additionally, there are no clear modulations at ~8–25 keV (as shown in Figure 3b).

3.3. Pitch Angle Spectrogram

Figure 4 shows the pitch angle distribution of ion energy flux in six different energy channels. We can see that there are steady periodic flux modulations and clear pitch angle dispersions with negative slope in these energy channels (~2–6 keV and ~50–75 keV). In each wave cycle, the peak (or valley) of flux has the largest time lag at 0° pitch angle and decreases with increasing pitch angle. This is another characteristic of drift-bounce resonance, which may be caused by the time of flight effect to the satellite in the Southern Hemisphere (MLAT ≈ −11°; Ren et al., 2017; Yang et al., 2011; Zhu et al., 2019).

3.4. Azimuthal Wave Number

Azimuthal wave number can be estimated by two methods: One is to analyze the phase delay between multiple satellites or ground magnetometers and radars (Shi et al., 2018; Takahashi et al., 2013; Tian et al., 2012) and the other is to use finite Larmor radius effects of energy flux at one satellite (Min et al., 2017; Takahashi et al., 2018). In this study, we use the second method, because only a single satellite (TH-E) detected this

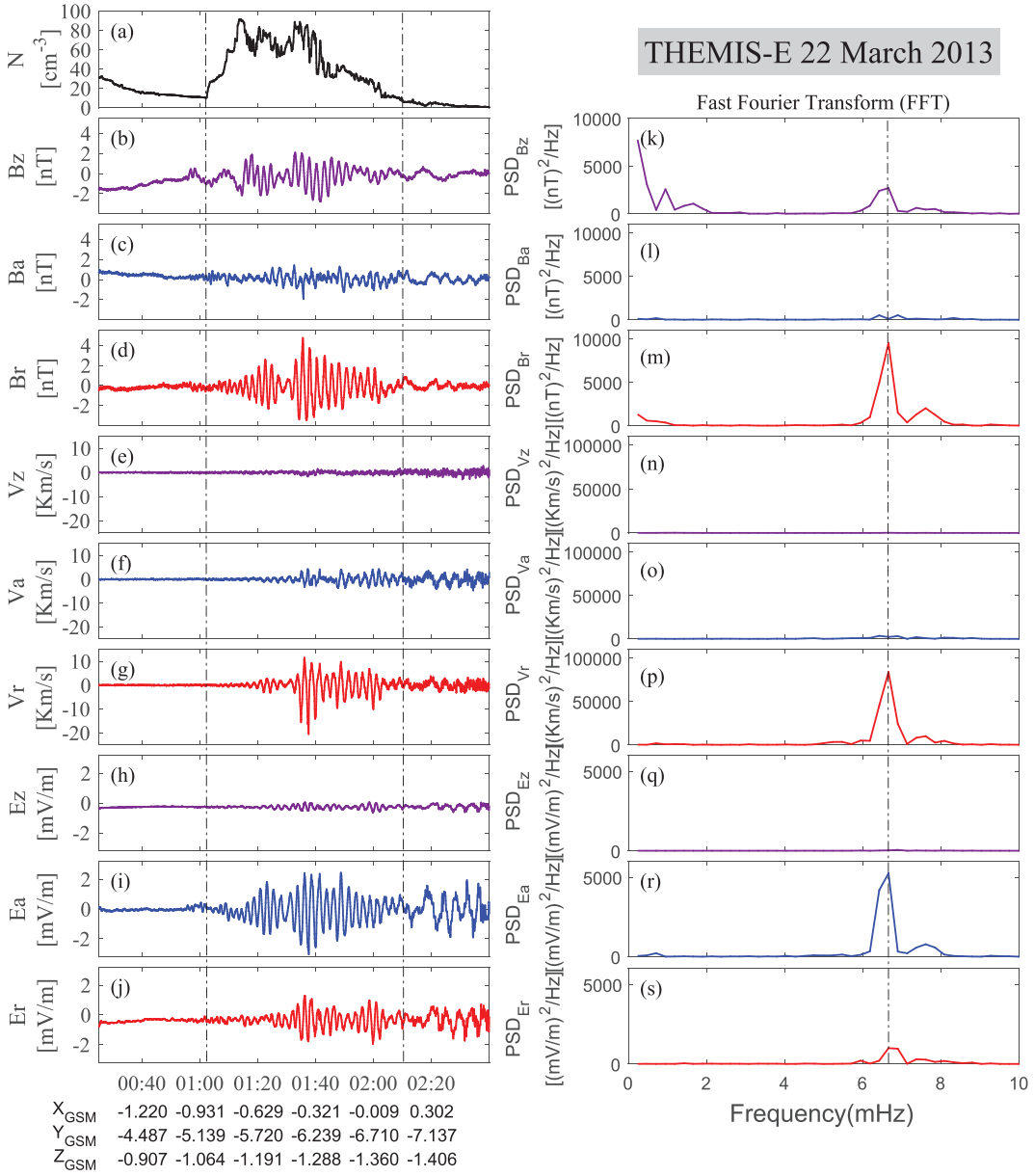

Figure 2. Observations by TH-E on 22 March 2013: (a) Electron density derived from the spacecraft potential measurement; (b–d) magnetic field components, (e–g) velocity components, and (h–j) electric field components in the FAC coordinate system; (k–s) FFT analysis to the components in corresponding left panels b–j.

wave event and no ground signal response was observed. This may be due to the highly localized wave structure and the ionospheric screening effect (Hughes & Southwood, 1976).

An observable gyrophase dependence in particle flux can develop at energies where the particle gyroradius ρ_L is comparable with the perpendicular wavelength ?$_\perp$ (Kivelson & Southwood, 1983). As shown in Figure 5 a, the gyrocenters of measured particles are located away from spacecraft by ρ_L, and they will be located in different phases of the wave for different gyrophases. Therefore, the spin modulation of the measured particle flux j can be expressed as (Min et al., 2017)

$$j \sim \exp\left(i\boldsymbol{k}_\perp \cdot \overrightarrow{\boldsymbol{\rho}_L} - i\omega t\right) \tag{2}$$

where $\boldsymbol{k}_\perp$ is the perpendicular wave number, $\overrightarrow{\boldsymbol{\rho}_L}$ is the vector form the spacecraft to the gyrocenter of measured particle, and ω is the wave frequency.

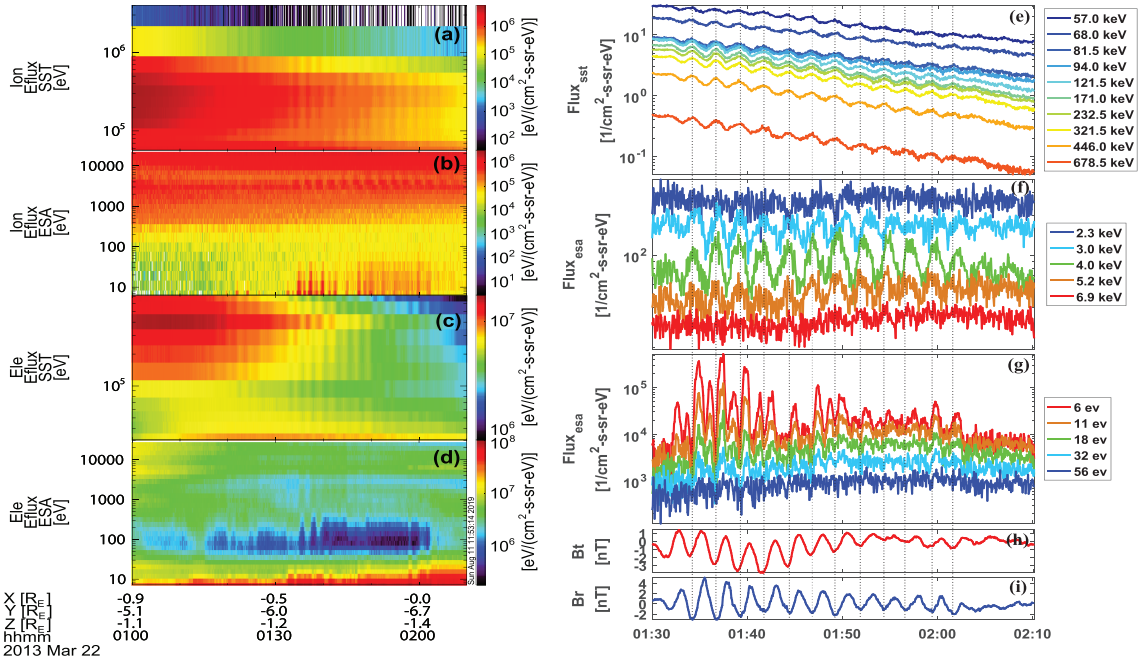

Figure 3. The omnidirectional energy spectrum and particle flux of ions and electrons. Panels a and b (c and d) are the energy spectrum for ions (electrons) measured by SST and ESA, respectively. Panels e–g show the ion flux at different energies. Panels h and i show the perturbation of total and radial magnetic field strength *Bt* and *Br*, respectively. The black lines in panels e–i indicate the location of the troughs in *Br*.

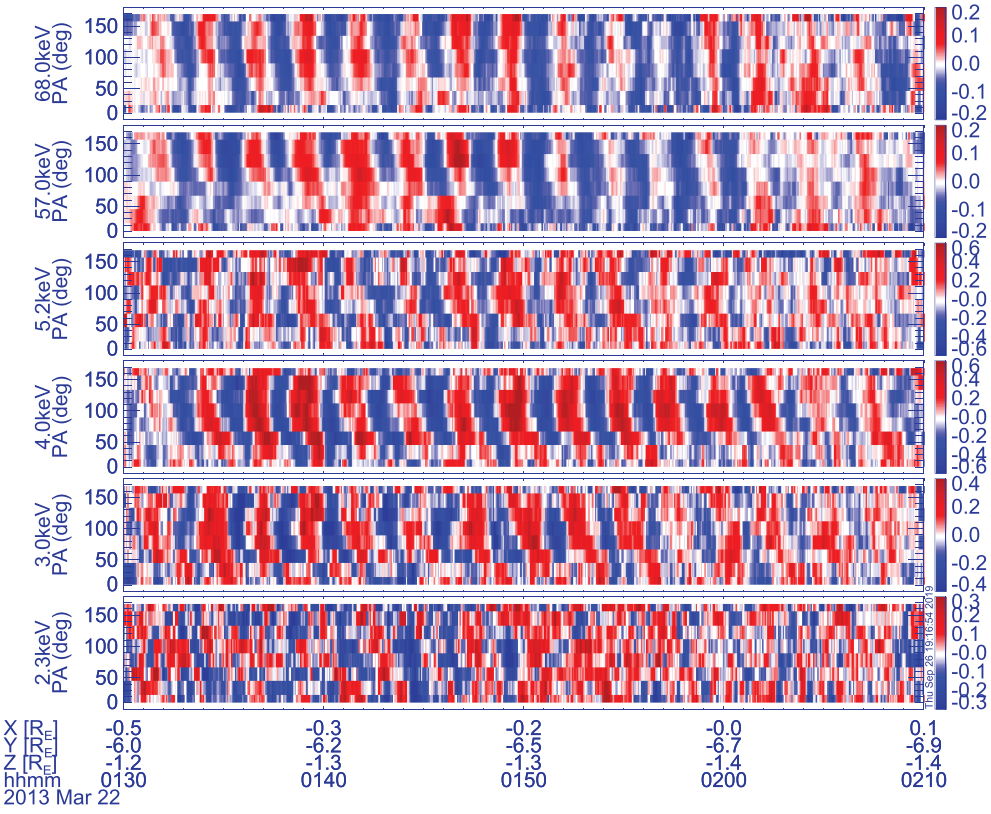

Figure 4. Pitch angle spectrogram for ions with different energies. The color indicates the residual flux $(J - J_0)/J_0$ (Hao et al., 2017), where J is the original energy flux measured by TH-E and J_0 is the 20-min running average of J.

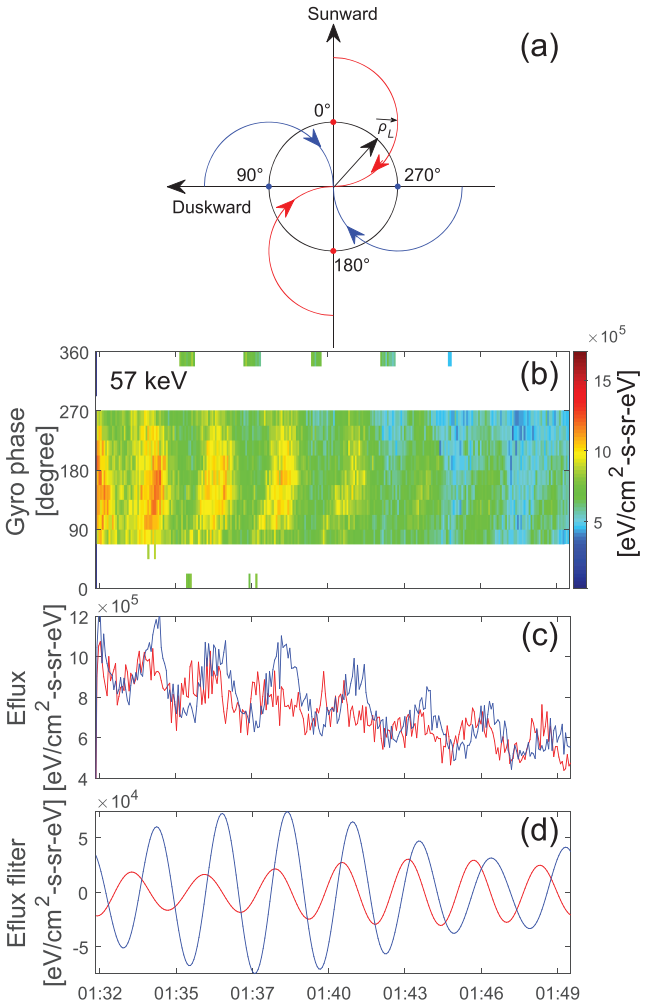

Figure 5. The finite Larmor radius effects shown in ion energy fluxes. (a) Illustration of measured particle from different look directions. The four lines represent the trajectories of particles with the guiding center located at 0°, 90°, 180°, and 270°. (b) Energy flux in different gyrophase for ions with 57 keV. (c) Energy flux of ions with the guiding center located at 90° (red) and 180° (blue). (d) Band-pass-filtered signals of energy flux in panel c.

Figure 5b shows the energy flux as a function of gyrophase near 90° pitch angle for ions with energy ~57 keV. We can see that there are clear periodic modulations, and the flux modulations are earlier at 90°(270°) than 180°, which indicates that the wave is propagating westward. Figure 5c shows the line plot of energy flux at 90° and 180° in Figure 5b, respectively. Figure 5d shows the band-pass-filtered results for the measurements in Figure 5c, and we can see that the average phase delay between the energy flux at 90° and 180° is $\tau \approx -38.6$s. From equation (2), we can estimate the wave number by calculating the phase delay τ in the 90° and 180° as $\tau\omega = k_{\perp}\cdot\rho_L$. Finally, assuming that the resonance ions are protons, the azimuthal wave number is calculated to be $m = k_{\perp}\cdot R \approx [-257, -216]$, where R is the distance from Earth's center to the spacecraft (as shown in supporting information Figures S1a–S1c). Moreover, it is clear that the fluxes are higher in the 90–180° sector than in 180–270° sector, which means that there is an inward radial gradient of ions of ~57 keV.

4. Discussion

4.1. Harmonic Mode

Figure 6 shows the process of analyzing harmonic mode of this poloidal wave event. In Figure 6b, the 5.7–7.7 mHz band-pass-filtered signals of radial magnetic field *Br* and azimuthal electric field *Ea* are plotted for this wave event. The phase differences between the band-pass-filtered *Br* and *Ea* are shown in the Figure 6c. We can find that the phase of *Br* leads *Ea* by ~90°. Because the satellite is located slightly south of the magnetic equator (MLAT ≈ −11°), this event can be identified as an even harmonic standing wave, as discussed in section 1. Furthermore, we also compare the observed wave frequency with the numerically calculated field line eigenfrequency (calculated following the method of Rankin et al., 2006, and Degeling et al., 2010), as shown in Figure 6d. In the numerical calculation, the background ions are considered as protons, and the mass density on the equatorial plane is retrieved from satellite measurements. We can see that the wave frequency of 6.7 mHz (dashed line) is close to the simulated second harmonic eigenfrequency (red line). Therefore, we confirm that the observed ULF waves in the plume are second harmonic poloidal oscillations. In addition, it is noteworthy that the second harmonic poloidal eigenfrequency decreases rapidly to the wave frequency at the beginning of Figure 6d. This is attributed to the sudden increase of the plasma density when TH-E enters the plume. Moreover, TH-A and TH-D detected 17.1 mHz second harmonic poloidal waves and 3.6 mHz fundamental toroidal waves, respectively. Their frequencies and wave modes are different from the wave detected by TH-E. This implies that the waves observed by TH-E may occur only in the plume and are localized second harmonic poloidal wave.

4.2. Wave-Particle Modulation

As shown in sections 3.2–3.3 (Figures 3f and 4), there are three different modulations between the wave and ions, including (1) the double peaks at lower energy ions (<32 eV), (2) the drift-bounce resonance at ~2–6 keV and ~50–75 keV, and (3) an antiphase modulation between *Br* and higher-energy particles (>75 keV). The first two modulations will be discussed in the following section, and the third modulation could be the result of the radial oscillation of the field line carrying particles with large inward flux gradient.

4.2.1. *E* Cross *B* Effect

Figure 7a shows the ion fluxes of lower energy ions (6 and 11 eV) in Figure 3g at 01:00–02:10 UT. It is clear that there are double peaks in each wave cycle, which are indicated by the vertical dashed lines. We calculated the increased particle energy produced by accounting for *E* cross *B* drift motion, as shown in Figure 7b.

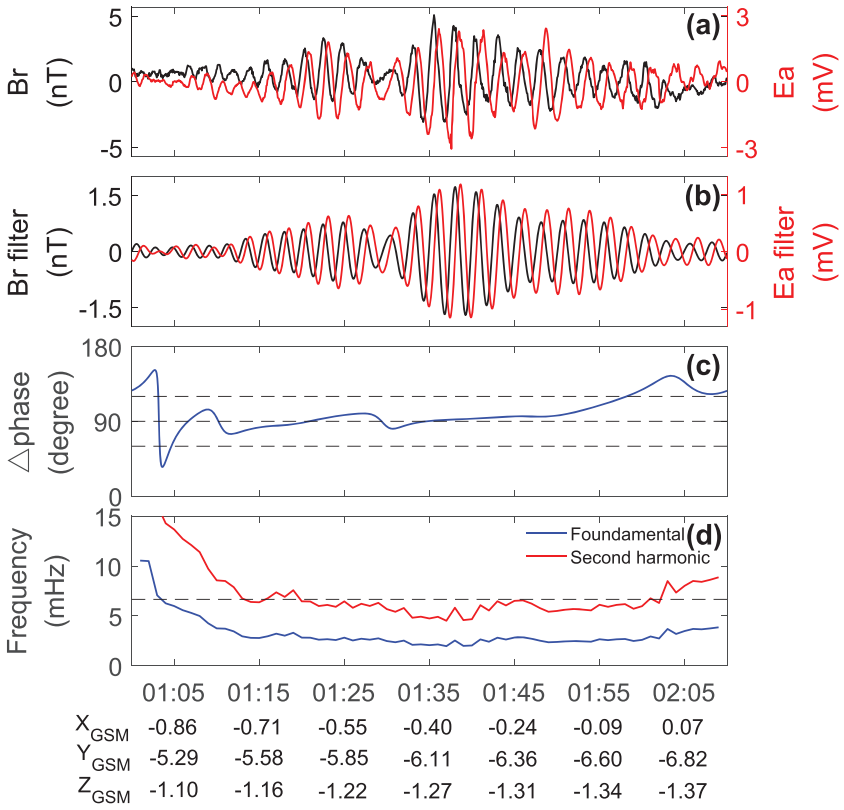

Figure 6. (a) The radial magnetic field *Br* (black) and azimuthal electric field *Ea* (red). (b) Band-pass-filtered (5.7 to 7.7 mHz) signals of *Br* and *Ea* in panel a. (c) The phase differences between the band-pass-filtered *Br* and *Ea*. The three black dashed lines indicate the 60°, 90°, and 120° phase differences, respectively. (d) The simulated fundamental poloidal eigenfrequency (blue) and second harmonic poloidal eigenfrequency (red), respectively.

We can see that the trend in Figure 7b is in good agreement with that in Figure 7a, which means that the double peaks are the results of the cold plasma in the plume being modulated by the observed wave through the *E* cross *B* effect.

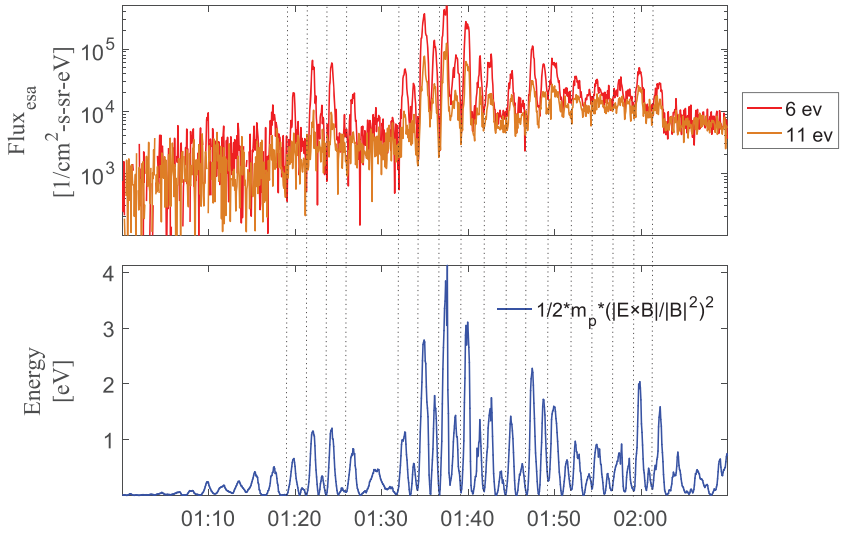

Figure 7. (a) Ion flux for energy of 6 and 11 eV, which is the same as that of Figure 3g during 01:00–02:10 UT, and (b) the calculated ion energy by *E* cross *B* effect. The black lines are the same as that in Figure 3.

4.2.2. Drift-Bounce Resonance

The theory of interaction between charged particles and ULF waves via the drift-bounce resonance has been well developed (Southwood, 1976; Southwood & Kivelson, 1981; Zhou et al., 2016). The condition of drift-bounce resonance can be expressed as

$$\omega - m\omega_d = N\,\omega_b \tag{3}$$

where ω is the wave angular frequency, ω_d is the particle drift angular frequency, ω_b is the particle bounce angular frequency, m is the azimuthal wave number, and N is an integer (e.g., $N = \pm 1$ representing the second harmonic mode; Southwood et al., 1969). The proton angular drift frequency ω_d and bounce frequency ω_b can be calculated based on the following equations (Chisham, 1996; Hamlin et al., 1961; Li et al., 1993):

$$\omega_b = \frac{\pi\sqrt{\frac{W}{2m_i}}}{LR_E(1.3 - 0.56sin\ \alpha)} \tag{4}$$

$$\omega_d = -\frac{3LWR_E(0.7 + 0.3sin\ \alpha)}{qk_0} + \frac{90(1 - 0.159K_P + 0.0093K_P{}^2)^{-3}L^3R_Esin\ \theta}{k_0} + \Omega_E \tag{5}$$

where W is particle energy, m_i is the ion mass, α is the particle's equatorial pitch angle, q is electric charge of particle, k_0 is the magnetic moment of Earth's dipole, R_E is the Earth's radius, Kp is the geomagnetic activity index,$\theta$is the azimuthal angle (θ = MLT/24 × 360), and Ω_E is the angular frequency of the Earth's rotation.

Therefore, we can calculate the drift-bounce resonance energy of ions for the observed 6.7 mHz second harmonic poloidal wave with m-number range of [−257, −216] at $L \approx 6.6$ and MLT ≈ 6 from equations (3)–(5). The calculated resonant energy is ~4.9 keV for $N = 1$ resonance of protons and 59.5–76 keV for $N = -1$ resonance of protons (as shown in supporting information Figure S1d). In this work, both the energy spectrum and the pitch angle distribution show that the drift-bounce resonance occurs at ~2–6 keV, which is consistent with the calculated resonant energy 4.9 keV for $N = 1$ proton resonance. The pitch angle distribution in Figure 4 also shows that the drift-bounce resonance exists at ~50–75 keV, which are also consistent with the calculated resonant energy 59.5–76 keV for $N = -1$ proton resonance. Unfortunately, we cannot prove the type of resonance particles more precisely because THEMIS satellite cannot distinguish the composition of particles.

4.3. Source of Free Energy

Several generation mechanisms can produce second harmonic Pc4-5 poloidal mode waves. Poloidal waves generated by an external source are usually global waves with a low m number, and a strong compressional component (Dai et al., 2015; Liu et al.,2013), which are different from the observations in this paper. We also checked the solar wind data (e.g., from the GEOTAIL satellite) and found no evidence supporting the excitation of the observed waves by an external source. For internal sources, it has been well accepted that second harmonic poloidal waves are frequently generated by the drift-bounce resonance. Whether a given drift-bounce resonance contributes to wave generation depends on the ion PSD and whether free energy in the particle distribution exists that can be transferred to the wave. The condition for instability is given by (Southwood & Hughes, 1983)

$$\frac{dF}{dW} = \left.\frac{\partial F}{\partial W}\right|_{M,L} + \left(\frac{dL}{dW}\right)\left.\frac{\partial F}{\partial L}\right|_{M,W} > 0, \frac{dL}{dW} \approx \frac{mR_EL^2}{q\omega k_0} \tag{6}$$

where F is the particle PSD, W is particle energy, M is the magnetic moment, q is electric charge of a particle, k_0 is the magnetic moment of Earth's dipole, and R_E is the Earth's radius. This equation indicates that both the bump-on-tail structure distribution (the first term) and a radial inward gradient of particles (the second term) could provide free energy to the generation of wave.

Figure 8a shows the PSD distribution of ions for different energies and pitch angles at L ~ 6.18. The thick black (red) lines in the figure are contours of constant magnetic moment for the resonant protons (Mres1 = 57 (keV) $\sin^2(90°)$/137 (nT) and Mres2 = 4 (keV) $\sin^2(90°)$/137 (nT)). Figure 8b shows the relationship between the PSD and energy along the thick black and red lines of Figure 8a. We can see that there are no obvious positive PSD gradients ($\partial F/\partial W|_{M,\,L} \sim -118\ s^3\ km^{-6}\ keV^{-1}$) for 4 keV, which means that this

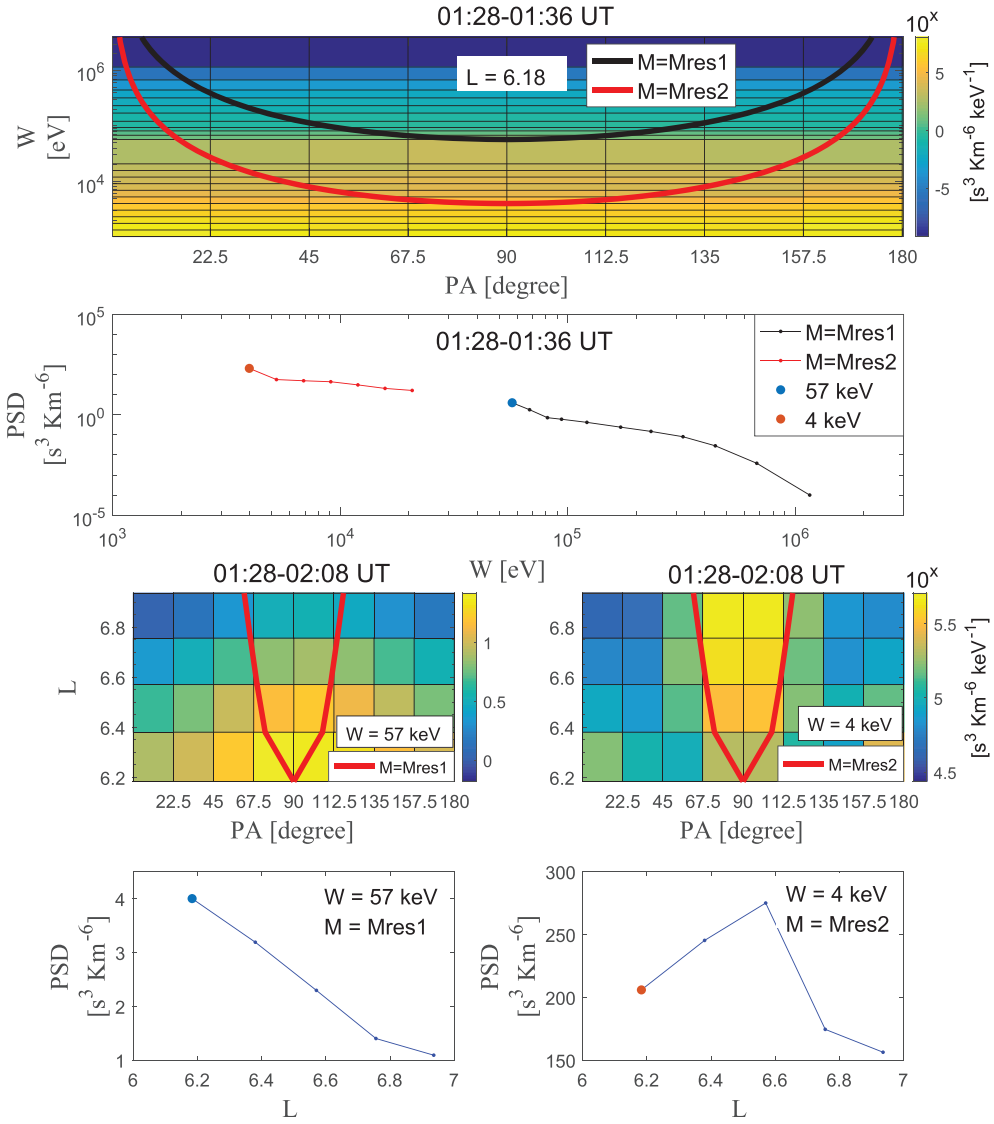

Figure 8. (a) Phase space density (PSD) for different energy and pitch angle. (b) PSD as a function of energy. (c, d) PSD of 57 and 4 keV ions for different L and pitch angle. (e, f) PSD as a function of L for ions with 57 and 4 keV.

wave event could not be generated by bump-on-tail distribution at low energy. Figures 8c and 8d show the PSD distribution of 57 and 4 keV ions for different L and pith angles. The thick red lines in the figure also are contours of constant magnetic moment. Figures 8e and 8f show the relationship between the PSD and L-shell along the red thick lines of Figures 8c and 8d. A significant inward gradient ($\partial F/\partial L|_{M,\ W} \sim -4.11$ s^3 km^{-6}) in the plume for 57 keV is shown in Figure 8e, which is consistent with the results of Figure 5. From equation (6), we find the following:

For 57 keV: $\frac{dF}{dW} = \frac{\partial F}{\partial W}\big|_{M,L} + \left(\frac{dL}{dW}\right)\frac{\partial F}{\partial L}\big|_{M,W} \sim -0.2 - 0.18 \times (-4.11)$

$$\sim 0.54\ \left(s^3 km^{-6} keV^{-1}\right) > 0.$$

For 4 keV: $\frac{dF}{dW} = \frac{\partial F}{\partial W}\big|_{M,L} + \left(\frac{dL}{dW}\right)\frac{\partial F}{\partial L}\big|_{M,W} \sim -118 - 0.18 \times 200$

$$\sim -154\ \left(s^3 km^{-6} keV^{-1}\right) < 0.$$

This suggests that the free energy for wave generation could be provided by the inward radial gradient of ~57 keV.

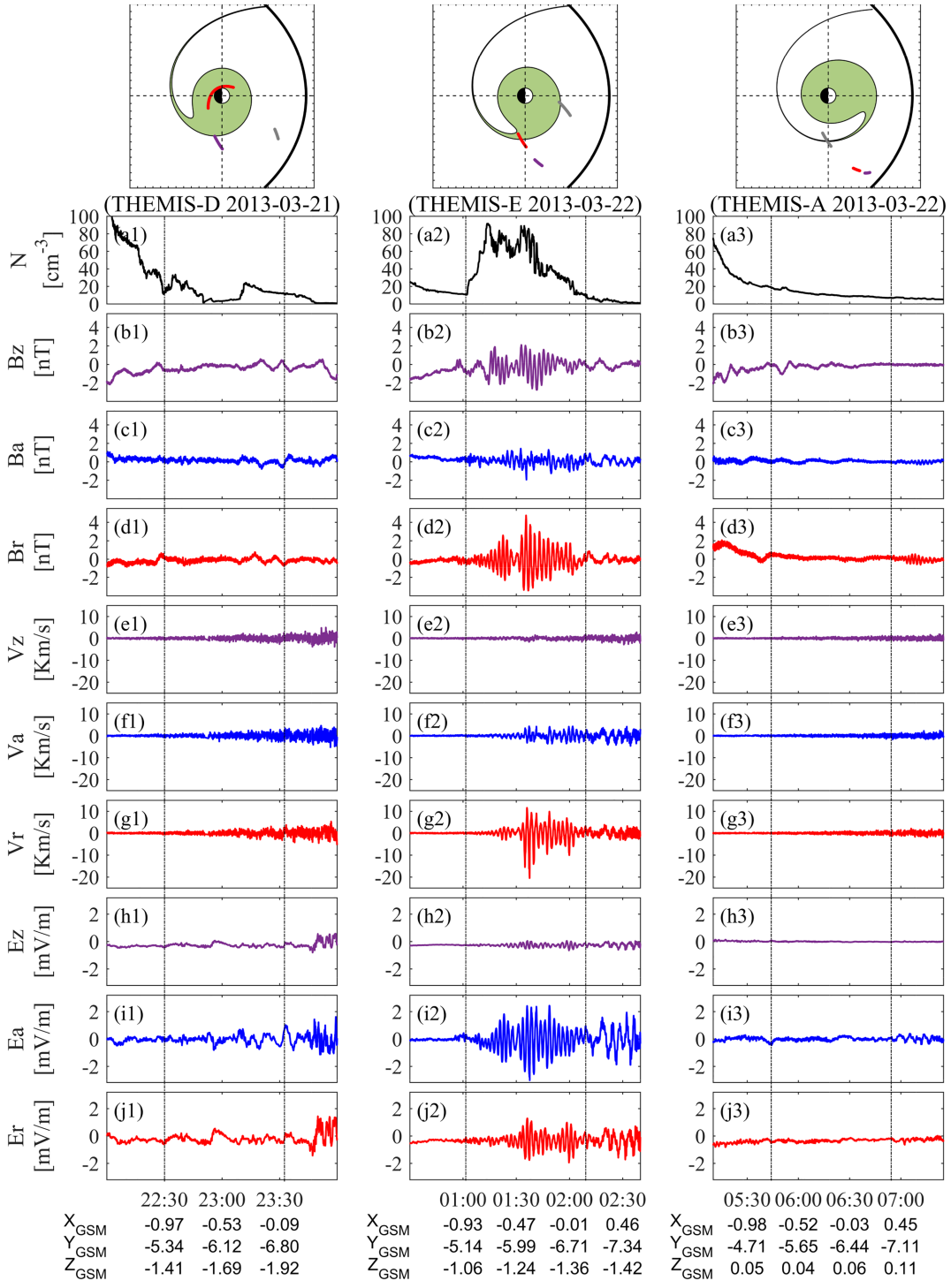

Figure 9. Orbits of TH-A (gray), TH-D (purple), and TH-E (red) and observations by TH-D, TH-E, and TH-A. (a) Electron density derived from the spacecraft potential measurement, (b–d) magnetic field components, (e–g) velocity components, and (h–j) electric field components in the FAC coordinate system.

4.4. The Effect of the Plume

Figure 9 shows the overviews of TH-D (left), TH-E (middle), and TH-A (right) in the region of this wave event. The top three panels show the orbits of TH-A (sienna), TH-D (purple), and TH-E (red) at different times. The green regions indicate the simulated plasmaspheric plume regions. Figures 9a–9j display the

electron density, magnetic field, velocity, and electric field components in the same format as Figures 2a–2j. We can see that TH-D and TH-A traversed through the same region 2h before and 3 hr later when there is no plume, and neither satellite observed waves. We also checked the PSD distributions of TH-D and TH-A and found that both of them detected similar radial inward gradient distribution near 57 keV with that of TH-E. These suggest that the existence of the ULF wave is likely associated with the observed plasmaspheric plume. The possible reason is that the standing ULF waves can only be observed at the locations where the drift-bounce resonance frequency matches the local eigenfrequency. In this study, we suggest that the high plasma density in the plasmaspheric plume plays a role in reducing the local eigenfrequency (as shown in Figure 6d) to match the drift-bounce frequency and excite the second harmonic poloidal oscillations in the dawnside.

5. Conclusion

High-m localized second harmonic poloidal oscillations were observed in a dawnside plasmaspheric plume. We find that the observed waves are likely generated by drift-bounce resonance with an inward radial gradient distribution at higher energy (~50–75 keV). These waves can also modulate particles through drift-bounce resonance at 2–6 keV and $E \times B$ effect at lower energy (<32 eV). In addition to the duskside plasmaspheric plume, this study confirms that the dense and cold plasma in the plasmaspheric plume controls the generation of Pc4-5 poloidal ULF waves on the dawnside by reducing the local field line eigenfrequency to the resonant frequency.

Acknowledgments
We acknowledge the THEMIS project team for THEMIS data at http://themis.ssl.berkeley.edu/ website. Specifically, we thank Goldstein, J., for the results of time-varying simulated plasmapause location at http://enarc.space.swri.edu/PTP/ website. The authors thank Jasmine Sandhu for valuable discussions in the preparation of this work. This work was supported by the Shandong University (Weihai) Future Plan for Young Scholars (2017WHWLJH08), the National Natural Science Foundation of China (Grants 41574157, 41774153, and 41961130382), the Science and Technology Facilities Council (Grant ST/N000722/1), and the Natural Environment Research Council (Grants NE/L007495/1, NE/P017150/1, and NE/P017185/1). Project Supported by the Specialized Research Fund for State Key Laboratories.

References

Allan, W., White, S. P., & Poulter, E. M. (1986). Impulse-excited hydromagnetic cavity and field-line resonances in the magnetosphere. *Planetary and Space Science*, *34*, 371–385. https://doi.org/10.1016/0032-0633(86)90144-3

Angelopoulos, V. (2008). The THEMIS mission. *Space Science Reviews*, *141*, 5–34. https://doi.org/10.1007/s11214-008-9336-1

Auster, H. U., Glassmeier, K. H., Magnes, W., Aydogar, O., Baumjohann, W., Constantinescu, D., et al. (2008). The THEMIS fluxgate magnetometer. *Space Science Reviews*, *141*, 235–264. https://doi.org/10.1007/s11214-008-9365-9

Bonnell, J. W., Mozer, F. S., Delory, G. T., Hull, A. J., Ergun, R. E., Cully, C. M., et al. (2008). The electric field instrument (EFI) for THEMIS. *Space Science Reviews*, *141*(1-4), 303–341. https://doi.org/10.1007/s11214-008-9469-2

Chappell, C. R. (1974). Detached plasma regions in the magnetosphere. *Journal of Geophysical Research*, *79*, 1861–1870. https://doi.org/10.1029/JA079i013p01861

Chappell, C. R., Harris, K. K., & Sharp, G. W. (1970). The morphology of the bulge region of the plasmasphere. *Journal of Geophysical Research*, *75*(19), 3848–3861. https://doi.org/10.1029/ja075i019p03848

Chisham, G. (1996). Giant pulsations: An explanation for their rarity and occurrence during geomagnetically quiet times. *Journal of Geophysical Research*, *101*(A11), 24,757–24,763. https://doi.org/10.1029/96JA02540

Claudepierre, S. G., Elkington, S. R., & Wiltberger, M. (2008). Solar wind driving of magnetospheric ULF waves. Pulsations driven by velocity shear at the magnetopause. *Journal of Geophysical Research*, *113*, A05218. https://doi.org/10.1029/2007JA012890

Dai, L., Takahashi, K., Lysak, R., Wang, C., Wygant, J. R., Kletzing, C., ... Chen, L. (2015). Storm time occurrence and spatial distribution of Pc4 poloidal ULF waves in the inner magnetosphere: A Van Allen Probes statistical study. *Journal of Geophysical Research: Space Physics*, *120*(6), 4748–4762. https://doi.org/10.1002/2015ja021134

Dai, L., Takahashi, K., Wygant, J. R., Chen, L., Bonnell, J., Cattell, C. A., et al. (2013). Excitation of poloidal standing Alfvén waves through drift resonance wave-particle interaction. *Geophysical Research Letters*, *40*, 4127–4132. https://doi.org/10.1002/grl.50800

Degeling, A. W., Rankin, R., Kabin, K., Rae, I. J., & Fenrich, F. R. (2010). Modeling ULF waves in a compressed dipole magnetic field. *Journal of Geophysical Research*, *115*, A10212. https://doi.org/10.1029/2010JA015410

Degeling, A. W., Rankin, R., & Zong, Q.-G. (2014). Modeling radiation belt electron acceleration by ULF fast mode waves, launched by solar wind dynamic pressure fluctuations. *Journal of Geophysical Research: Space Physics*, *119*, 8916–8928. https://doi.org/10.1002/2013JA019672

Fu, S. Y., & Sun, W. J. (2016). Models of the Earth's plasmapause position. *Science China Earth Sciences*, *59*(4), 871–872. https://doi, https://doi.org/10.1007/s11430-016-5266-z

Glassmeier, K.-H., Buchert, S., Motschmann, U., Korth, A., & Pedersen, A. (1999). Concerning the generation of geomagnetic giant pulsations by drift-bounce resonance ring current instabilities. *Annales Geophysicae*, *17*(3), 338–350. https://doi.org/10.1007/s00585-999-0338-4

Goldstein, J., Pascuale, S. D., Kletzing, C., Kurth, W., Genestreti, K. J., Skoug, R. M., et al. (2014). Simulation of Van Allen Probes plasmapause encounters. *Journal of Geophysical Research: Space Physics*, *119*, 7464. https://doi.org/10.1002/2014JA020252

Goldstein, J., Sandel, B. R., Forrester, M. F., Thomsen, T. F., & Hairston, M. R. (2005). Global plasmasphere evolution 22–23 April 2001. *Journal of Geophysical Research*, *110*, A12218. https://doi.org/10.1029/2005JA011282

Hamlin, D. A., Karplus, R., Vik, R. C., & Watson, K. M. (1961). Mirror and azimuthal drift frequencies for geomagnetically trapped particles. *Journal of Geophysical Research*, *66*(1), 1–4. https://doi.org/10.1029/JZ066i001p00001

Hao, Y. X., Zong, Q.-G., Wang, Y. F., Zhou, X.-Z., Zhang, H., Fu, S. Y., et al. (2014). Interactions of energetic electrons with ULF waves triggered by interplanetary shock: Van Allen Probes observations in the magnetotail. *Journal of Geophysical Research: Space Physics*, *119*, 8262–8273. https://doi.org/10.1002/2014JA020023

Hao, Y. X., Zong, Q.-G., Zhou, X.-Z., Rankin, R., Chen, X. R., Liu, Y., et al. (2017). Relativistic electron dynamics produced by azimuthally localized poloidal mode ULF waves: Boomerang-shaped pitch angle evolutions. *Geophysical Research Letters*, *44*, 7618–7627. https://doi.org/10.1002/2017GL074006

Hartinger, M., Turner, D., Plaschke, F., Angelopoulos, V., & Singer, H. (2013). The role of transient ion foreshock phenomena in driving Pc5 ULF wave activity. *Journal of Geophysical Research: Space Physics*, *118*, 299–312. https://doi.org/10.1029/2012JA018349

Hughes, W. J., & Southwood, D. J. (1976). The screening of micropulsation signals by the atmosphere and ionosphere. *Journal of Geophysical Research*, *81*(19), 3234–3240. https://doi.org/10.1029/JA081i019p03234

Kivelson, M. G., & Southwood, D. J. (1983). Charged particle behavior in low-frequency geomagnetic pulsations: 3. Spin phase dependence. *Journal of Geophysical Research*, *88*(A1), 174. https://doi.org/10.1029/JA088ia01p00174

Larson, D., Moreau, T., Lee, R., Canario, R., & Lin, R. P. (2008). The solid state telescope for THEMIS. *Space Science Reviews*.

Lee, D., & Lysak, R. L. (1989). Magnetospheric ULF wave coupling in the dipole model: The impulsive excitation. *Journal of Geophysical Research*, *94*, 17097–17103. https://doi.org/10.1029/JA094iA12p17097

Li, X., Hudson, M., Chan, A., & Roth, I. (1993). Loss of ring current O^+ ions due to interaction with Pc5 waves. *Journal of Geophysical Research*, *98*, 215. https://doi.org/10.1029/92JA01540

Ling, Y., Shi, Q. Q., Shen, X.-C., Tian, A. M., Li, W. Y., Tang, B. B., et al. (2018). Observations of Kelvin-Helmholtz waves in the Earth's magnetotail near the lunar orbit. *Journal of Geophysical Research: Space Physics*, *123*, 3836–3847. https://doi.org/10.1029/2018JA025183

Liu, W., Cao, J. B., Li, X., Sarris, T. E., Zong, Q.-G., Hartinger, M., et al. (2013). Poloidal ULF wave observed in the plasmasphere boundary layer. *Journal of Geophysical Research: Space Physics*, *118*, 4298–4307. https://doi.org/10.1002/jgra.50427

Mcfadden, J. P., Carlson, C. W., Larson, D., Bonnell, J., Mozer, F., Angelopoulos, V., et al. (2008). THEMIS ESA first science results and performance issues. *Space Science Reviews*, *141*(1-4), 477–508. https://doi.org/10.1007/s11214-008-9433-1

Min, K., Takahashi, K., Ukhorskiy, A. Y., Manweiler, J. W., Spence, H. E., Singer, H., et al. (2017). Second harmonic poloidal waves observed by Van Allen Probes in the dusk-midnight sector. *Journal of Geophysical Research: Space Physics*, *122*, 3013–3039. https://doi.org/10.1002/2016JA023770

Oimatsu, S., Nosé, M., Takahashi, K., Yamamoto, K., Keika, K., Kletzing, C. A., et al. (2018). Van Allen Probes observations of drift-bounce resonance and energy transfer between energetic ring current protons and poloidal Pc4 wave. *Journal of Geophysical Research: Space Physics*, *123*, 3421–3435. https://doi.org/10.1029/2017JA025087

Rae, I. J., Donovan, E. F., Mann, I. R., Fenrich, F. R., Watt, C. E. J., Milling, D. K., et al. (2005). Evolution and characteristics of global Pc5 ULF waves during a high solar wind speed interval. *Journal of Geophysical Research*, *110*, A12211. https://doi.org/10.1029/2005JA011007

Rankin, R., Kabin, K., & Marchand, R. (2006). Alfvenic field line resonances in arbitrary magnetic field topology. *Advances in Space Research*, *38*(8), 1720–1729. https://doi.org/10.1016/j.asr.2005.09.034

Ren, J., Zong, Q. G., Zhou, X. Z., Rankin, R., Wang, Y. F., Gu, S. J., & Zhu, Y. F. (2017). Phase relationship between ULF waves and drift-bounce resonant ions: A statistical study. *Journal of Geophysical Research: Space Physics*, *122*, 7087–7096. https://doi.org/10.1002/2016JA023848

Rostoker, G., Lam, H.-L., & Olson, J. V. (1979). Pc 4 giant pulsations in the morning sector. *Journal of Geophysical Research*, *84*, 5153–5166. https://doi.org/10.1029/JA084iA09p05153

Sakurai, T., Tonegawa, Y., Kitagawa, T., Nowada, M., Yamawaki, A., Mukai, T., et al. (2014). Double-frequency oscillations of low energy plasma associated with transverse Pc 5 pulsations: GEOTAIL satellite observations. *Earth, Planets and Space*, *51*(1), 43–53. https://doi.org/10.1186/BF03352208

Shen, X. C., Shi, Q. Q., Zong, Q.-G., Tian, A. M., Nowada, M., Sun, W. J., et al. (2017). Dayside magnetospheric ULF wave frequency modulated by a solar wind dynamic pressure negative impulse. *Journal of Geophysical Research: Space Physics*, 122. https://doi.org/10.1002/2016JA023351

Shen, X.-C., Shi, Q. Q., Wang, B., Zhang, H., Hudson, M. K., Nishimura, Y., et al. (2018). Dayside magnetospheric and ionospheric responses to a foreshock transient on 25 June 2008: 1. FLR observed by satellite and ground-based magnetometers. *Journal of Geophysical Research: Space Physics*, *123*, 6335–6346. https://doi.org/10.1029/2018JA025349

Shen, X. C., Zong, Q.-G., Shi, Q. Q., Tian, A. M., Sun, W. J., Wang, Y. F., et al. (2015). Magnetospheric ULF waves with increasing amplitude related to solar wind dynamic pressure changes: The Time History of Events and Macroscale Interactions during Substorms (THEMIS) observations. *Journal of Geophysical Research: Space Physics*, *120*, 7179–7190. https://doi.org/10.1002/2014JA020913

Shi, Q. Q., Hartinger, M. D., Angelopoulos, V., Tian, A. M., Fu, S. Y., Zong, Q.-G., et al. (2014). Solar wind pressure pulse-driven magnetospheric vortices and their global consequences. *Journal of Geophysical Research: Space Physics*, *119*, 4274–4280. https://doi.org/10.1002/2013ja019551

Shi, Q. Q., Hartinger, M. D., Angelopoulos, V., Zong, Q.-G., Zhou, X.-Z., Zhou, X.-Y., et al. (2013). THEMIS observations of ULF wave excitation in the nightside plasma sheet during sudden impulse events. *Journal of Geophysical Research: Space Physics*, *118*, 284–298. https://doi.org/10.1029/2012JA017984

Shi, X., Baker, J. B. H., Ruohoniemi, J. M., Hartinger, M. D., Murphy, K. R., Rodriguez, J. V., et al. (2018). Long-lasting poloidal ULF waves observed by multiple satellites and high-latitude SuperDARN radars. *Journal of Geophysical Research: Space Physics*, *123*(10), 8422–8438. https://doi.org/10.1029/2018JA026003

Shue, J.-H., Song, P., Russell, C. T., Steinberg, J. T., Chao, J. K., Zastenker, G., et al. (1998). Magnetopause location under extreme solar wind conditions. *Journal of Geophysical Research*, *103*, 17691–17700. https://doi.org/10.1029/98JA01103

Singer, H. J., Hughes, J. W., & Russell, C. T. (1982). Standing hydromagnetic waves observed by ISEE 1 and 2: Radial extent and harmonic. *Journal of Geophysical Research*, *87*(A5), 3519–3529. https://doi.org/10.1029/JA087iA05p03519

Southwood, D. J. (1976). A general approach to low-frequency instability in the ring current plasma. *Journal of Geophysical Research*, *81*, 3340–3348. https://doi.org/10.1029/JA081i019p03340

Southwood, D. J., Dungey, J. W., & Etherington, R. J. (1969). Bounce resonant interaction between pulsations and trapped particles. *Planetary and Space Science*, *17*(3), 349–361. https://doi.org/10.1016/0032-0633(69)90068-3

Southwood, D. J., & Hughes, W. J. (1983). Theory of hydromagnetic waves in the magnetosphere. *Space Science Reviews*, *35*(4). https://doi.org/10.1007/bf00169231

Southwood, D. J., & Kivelson, M. G. (1981). Charged particle behavior in low-frequency geomagnetic pulsations: I. Transverse waves. *Journal of Geophysical Research*, *86*, 5643–5657. https://doi.org/10.1029/ja086ia07p05643

Spasojević, M., Goldstein, J., Carpenter, D. L., Inan, U. S., Sandel, B. R., Moldwin, M. B., & Reinisch, B. W. (2003). Global response of the plasmasphere to a geomagnetic disturbance. *Journal of Geophysical Research*, *108*(A9), 1340. https://doi.org/10.1029/2003JA009987

Takahashi, K., Denton, R. E., Hirahara, M., Min, K., Ohtani, S., & Sanchez, E. (2014). Solar cycle variation of plasma mass density in the outer magnetosphere: Magnetoseismic analysis of toroidal standing Alfvén waves detected by Geotail. *Journal of Geophysical Research: Space Physics*, *119*, 8338–8356. https://doi.org/10.1002/2014JA020274

Takahashi, K., Glassmeier, K.-H., Angelopoulos, V., Bonnell, J., Nishimura, Y., Singer, H. J., & Russell, C. T. (2011). Multisatellite observations of a giant pulsation event. *Journal of Geophysical Research*, *116*, A11223. https://doi.org/10.1029/2011JA016957

Takahashi, K., Hartinger, M. D., Angelopoulos, V., Glassmeier, K.-H., & Singer, H. J. (2013). Multispacecraft observations of fundamental poloidal waves without ground magnetic signatures. *Journal of Geophysical Research: Space Physics*, *118*, 4319–4334. https://doi.org/10.1002/jgra.50405

Takahashi, K., Oimatsu, S., Nosé, M., Min, K., Claudepierre, S. G., Chan, A., et al. (2018). Van Allen Probes observations of second-harmonic poloidal standing Alfvén waves. *Journal of Geophysical Research: Space Physics*, *123*, 611–637. https://doi.org/10.1002/2017JA024869

Tian, A. M., Shen, X. C., Shi, Q. Q., Tang, B. B., Nowada, M., Zong, Q. G., & Fu, S. Y. (2016). Dayside magnetospheric and ionospheric responses to solar wind pressure increase: Multispacecraft and ground observations. *Journal of Geophysical Research: Space Physics*, *121*, 10,813–10,830. https://doi.org/10.1002/2016JA022459

Tian, A. M., Zong, Q. G., Zhang, T. L., Nakamura, R., Du, A. M., Baumjohann, W., et al. (2012). Dynamics of long-period ULF waves in the plasma sheet: Coordinated space and ground observations. *Journal of Geophysical Research*, *117*, A03211. https://doi.org/10.1029/2011JA016551

Wang, C., Rankin, R., Wang, Y., Zong, Q.-G., Zhou, X., Takahashi, K., et al. (2018). Poloidal mode wave-particle interactions inferred from Van Allen Probes and CARISMA ground-based observations. *Journal of Geophysical Research: Space Physics*, *123*, 4652–4667. https://doi.org/10.1029/2017JA025123

Yamamoto, K., Nosé, M., Kasahara, S., Yokota, S., Keika, K., Matsuoka, A., et al. (2018). Giant pulsations excited by a steep earthward gradient of proton phase space density: Arase observation. *Geophysical research Letters*, 45. https://doi.org/10.1029/2018GL078293

Yang, B., Zong, Q.-G., Fu, S. Y., Takahashi, K., Li, X., Wang, Y. F., et al. (2011). Pitch angle evolutions of oxygen ions driven by storm time ULF poloidal standing waves. *Journal of Geophysical Research*, *116*, A03207. https://doi.org/10.1029/2010JA016047

Yang, B., Zong, Q.-G., Wang, Y. F., Fu, S. Y., Song, P., Fu, H. S., et al. (2010). Cluster observations of simultaneous resonant interactions of ULF waves with energetic electrons and thermal ion species in the inner magnetosphere. *Journal of Geophysical Research*, *115*, A02214. https://doi.org/10.1029/2009JA014542

Zhang, S., Tian, A., Shi, Q., Li, H., Degeling, A. W., Rae, I. J., et al. (2018). Statistical study of ULF waves in the magnetotail by THEMIS observations. *Annales Geophysicae*, *36*, 1335–1346. https://doi.org/10.5194/angeo-36-1335-2018

Zhou, X.-Z., Wang, Z.-H., Zong, Q.-G., Rankin, R., Kivelson, M. G., Chen, X.-R., et al. (2016). Charged particle behavior in the growth and damping stages of ultralow frequency waves: Theory and Van Allen Probes observations. *Journal of Geophysical Research: Space Physics*, *121*, 3254–3263. https://doi.org/10.1002/2016JA022447

Zhu, Y. F., Gu, S.-J., Zhou, X. Z., Zong, Q.-G., Ren, J., Sun, X. R., et al. (2019). Drift-bounce resonance between charged particles and ultra-low frequency waves: Theory and Observations. *Journal of Geophysical Research: Space Physics*.

Zong, Q.-G., Wang, Y. F., Zhang, H., Fu, S. Y., Zhang, H., Wang, C. R., et al. (2012). Fast acceleration of inner magnetospheric hydrogen and oxygen ions by shock induced ULF waves. *Journal of Geophysical Research*, *177*, A11206. https://doi.org/10.1029/2012JA018024